https://doi.org/10.62836/iaet.v5i1.0004

Global Science Publishing

IAET

Innovations in Applied Engineering and Technology

https://ojs.sgsci.org/journals/iaet

Article

Sensorless Control of PMSM across the Full Speed Range Based on Fuzzy Logic

Jin Dai [1], Haichao Liu [1] and Likang Fan [2,*]

[1] *Fulin Precision Machining Co, Ltd., Mianyang 621050, China*

[2] *School of Automobile and Transportation, Xihua University, Pidu District, Chengdu 610039, China*

Abstract: To realize full-speed-range operation of the permanent magnet synchronous motor (PMSM) under sensorless control, this paper presents a full-speed-domain sensorless control scheme that relies on fuzzy-logic-based switching between high-frequency injection (HFI) and sliding mode observer (SMO). The core concept is to apply HFI within the zero-low speed region and transition to SMO once the rotor enters the medium-high speed region. To mitigate the chattering inherent in the conventional SMO, an improved SMO incorporating a hyperbolic tangent function together with an adaptive sliding mode gain is developed; meanwhile, a normalized quadrature phase-locked loop is adopted to recover the rotor position and speed, which raises the observation accuracy of the motor angle and speed. Furthermore, to refine the switching process, a fuzzy logic controller is embedded to online tune the weighting factors of HFI and SMO throughout the transition, thereby guaranteeing a smooth handover between the two control schemes. Simulation results indicate that the proposed approach can accomplish stable strategy switching. Relative to conventional switching techniques, the proposed strategy narrows the motor speed error by roughly 50% under no load and by roughly 30% under load. Hardware experiments further confirm the validity of the proposed method, cutting speed fluctuation during switching by approximately 35%.

Keywords: HFI; SMO; fuzzy logic; full speed domain sensorless control

1. Introduction

In applications including new energy vehicles and industrial automation, permanent magnet synchronous motors (PMSM) have seen rapid development owing to high reliability and simple structure. PMSM mainly adopt three control strategies, namely constant V/F control, direct torque control (DTC) [1] and field-oriented control (FOC) [2], with FOC being the most prevalently utilized one. In FOC, the rotor position information acts as the critical information of the whole control system. Accordingly, two control categories have emerged: sensored control and sensorless control. Sensored control acquires rotor position information through mechanical encoders or Hall sensors; nevertheless, the installation of position sensors brings about drawbacks such as bulky volume, elevated cost, and weak anti-interference capability. Hence, in recent years, numerous researchers have turned to the study of sensorless control, also referred to as position sensorless control [3].

The most widely used sensorless control algorithms are mainly founded on back-EMF, including the Luenberger observer [4], sliding mode observer (SMO) [5], and extended Kalman filter (EKF) [6]. These approaches depend chiefly on accurate extraction and processing the back-EMF. In the low-speed region, the

Received: 7 July 2026; Accepted: 22 July 2026.

* Corresponding: Likang Fan (BITfanlikang@163.com)

observer is unable to accurately observe the back-EMF. Therefore, open-loop control and approaches based on the rotor saliency effect are generally adopted [7].

Open-loop control mainly includes V/F and I/F control. V/F uses a fixed voltage vector and a fixed frequency as the input to the FOC control system. By adding a PID current loop to the V/F mode, the I/F algorithm can be constructed [8]. Nevertheless, open-loop control methods typically suffer from low control accuracy, sluggish dynamic response, and an inability to dynamically adjust. Therefore, to enhance motor performance in the zero-low speed domains, Kumar et al. [9] proposed an adaptive self-tuning algorithm for high-frequency injection (HFI), which performs online estimation and tuning of the high-frequency tracking loop gain. Yua et al. [10] put forward a pulsating high-frequency square-wave voltage injection strategy, which utilizes square-wave voltage carriers to implement high-frequency signal injection. These approaches allow closed-loop operation of the motor in the zero-low speed regions; however, to accomplish sensorless operation over the full-speed domain, one must integrate the algorithms of both the zero-low speed and medium-high speed regions. Bowen et al. [11] proposed a hybrid control strategy that uses I/F control for low-speed startup and shifts to a back-EMF position observer once the speed reaches a preset threshold. These methods are computationally simple and easy to implement, yet the system exhibits poor disturbance rejection capability during switching.

To accomplish smooth operation of the PMSM over the full speed domain, this paper puts forward a full-speed domain sensorless control algorithm: High-frequency signal injection (HFI) is utilized for zero-low speed operation, while the sliding mode observer (SMO) takes over when the motor runs at medium-high rotor speeds. Meanwhile, to overcome the chattering problem of the conventional SMO, the conventional sign function in SMO is replaced by a hyperbolic tangent function, thereby reducing chattering; adaptive sliding mode gains are utilized for additional chattering attenuation, and rotor position as well as rotational speed signals are extracted via a normalized quadrature phase-locked loop, enhancing the estimation precision of both electrical angle and rotor speed. To attain smooth switching between the two distinct control schemes, a fuzzy logic controller is designed to obtain the weight coefficients of the two observers during the transition, thus enabling a smooth handover of the sensorless algorithm during switching.

2. IPMSM Mathematical Model

Interior permanent magnet synchronous motors (IPMSMs) serve as the main research object of this paper, and a series of prerequisites are put forward before constructing the fundamental mathematical model:

(1) The magnetic circuit saturation of the PMSM core is neglected.

(2) There are no eddy current or hysteresis losses in the motor.

(3) The motor currents are symmetrical three-phase sinusoidal waveforms.

With the above idealized assumptions taken into consideration, the voltage equation for IPMSM in the rotary coordinate system is derived as:

$$\begin{bmatrix} u_d \\ u_q \end{bmatrix} = \begin{bmatrix} R_s & -\omega_e L_q \\ \omega_e L_d & R_s \end{bmatrix} \begin{bmatrix} i_d \\ i_q \end{bmatrix} + \begin{bmatrix} L_d & 0 \\ 0 & L_q \end{bmatrix} \frac{d}{dt} \begin{bmatrix} i_d \\ i_q \end{bmatrix} + \begin{bmatrix} 0 \\ \omega_e \psi_f \end{bmatrix} \tag{1}$$

where: u_d, u_q and i_d, i_q are the $d-q$ axis voltage and current, respectively; R_s is the stator resistance; L_d, L_q are the inductances, respectively; ω_e is the motor electrical angular velocity; ψ_e is the permanent magnet flux linkage.

$$\begin{bmatrix} u_\alpha \\ u_\beta \end{bmatrix} = \begin{bmatrix} R_s + \lambda L_d & -\omega_e\left(L_d - L_q\right) \\ -\omega_e\left(L_d - L_q\right) & R_s + \lambda L_q \end{bmatrix} \begin{bmatrix} i_\alpha \\ i_\beta \end{bmatrix} + \begin{bmatrix} e_\alpha \\ e_\beta \end{bmatrix} \tag{2}$$

where: u_α, u_β is the $\alpha-\beta$ axis voltage; $\lambda = d/dt$ is the differential operator; e_α, e_β is the extended back-EMF, satisfying the following equation:

$$\begin{bmatrix} e_\alpha \\ e_\beta \end{bmatrix} = \left[\left(L_d - L_q\right)\left(\omega_e i_d - \lambda i_q\right) + \omega_e \psi_f\right] \begin{bmatrix} -\sin\theta_e \\ \cos\theta_e \end{bmatrix} \tag{3}$$

3. Sensorless Control Algorithm

3.1. Pulsating High-Frequency Voltage Injection Method

The pulsating high-frequency voltage injection approach injects a high-frequency sinusoidal voltage signal solely on the d-axis of the estimated synchronous rotating $d-q$ coordinate system. Since the frequency of the high-frequency injection voltage substantially outpaces the fundamental frequency, the resistance term within the voltage equation becomes negligible compared to the reactance at high frequencies. This allows us to discard fundamental-frequency-related terms and simplify the IPMSM mathematical model as shown below:

$$\begin{cases} u_{din} \approx L_d \dfrac{di_{din}}{dt} \\ u_{qin} \approx L_q \dfrac{di_{qin}}{dt} \end{cases} \tag{4}$$

The rotor estimation error angle is defined as:

$$\theta_s = \theta - \theta_e \tag{5}$$

where θ denotes the actual rotor angle, and θ_e denotes the estimated rotor angle.

Within the estimated synchronous coordinate system aligned with the rotor, the mathematical relation linking high-frequency voltage and current is expressed by:

$$\begin{bmatrix} \dfrac{d\hat{i}_{dhfi}}{dt} \\ \dfrac{d\hat{i}_{qhfi}}{dt} \end{bmatrix} = A^{-1} \begin{bmatrix} \dfrac{1}{L_d} & 0 \\ 0 & \dfrac{1}{L_q} \end{bmatrix} A \begin{bmatrix} \hat{u}_{dhfi} \\ \hat{u}_{qhfi} \end{bmatrix} \tag{6}$$

where A denotes the rotation matrix, defined as:

$$A = \begin{bmatrix} \cos\theta_s & \sin\theta_s \\ -\sin\theta_s & \cos\theta_s \end{bmatrix} \tag{7}$$

By combining the above equations, one obtains:

$$\begin{cases} \dfrac{d\hat{i}_{dfhi}}{dt} = \dfrac{\left(L + \Delta L \cos 2\theta_s\right)\hat{u}_{dhfi} + \Delta L \hat{u}_{qhfi} \sin 2\theta_s}{L^2 - \Delta L^2} \\ \dfrac{d\hat{i}_{qhfi}}{dt} = \dfrac{\left(L - \Delta L \cos 2\theta_s\right)\hat{u}_{qhfi} + \Delta L \hat{u}_{dhfi} \sin 2\theta_s}{L^2 - \Delta L^2} \end{cases} \tag{8}$$

where L, ΔL denote the average inductance and half-difference inductance, respectively, defined as:

$$\begin{cases} L = \dfrac{L_q + L_d}{2} \\ \Delta L = \dfrac{L_q - L_d}{2} \end{cases} \tag{9}$$

For the pulsating high-frequency injection strategy, high-frequency sinusoidal voltage is injected into the d-axis belonging to the estimated synchronous rotation coordinate system.

$$\begin{cases} \hat{u}_{dhfi} = u_{hfi} \cos \omega_{hfi} t \\ \hat{u}_{qhfi} = 0 \end{cases} \tag{10}$$

Where u_{hfi} is the amplitude of the high-frequency voltage signal, and ω_{hfi} is the frequency of the high-frequency voltage signal.

By substituting Equation (10) into Equation (8), the motor current response at high frequency can be calculated as:

$$\begin{cases} i_{dhfi} = \dfrac{u_{hfi} \sin \omega_{hfi} t}{\omega_{hfi}\left(L^2 - \Delta L^2\right)}\left(L + \Delta L \cos 2\theta_s\right) \\ i_{qhfi} = \dfrac{u_{hfi} \sin \omega_{hfi} t}{\omega_{hfi}\left(L^2 - \Delta L^2\right)}\left(\Delta L \sin 2\theta_s\right) \end{cases} \tag{11}$$

A difference between d-axis and q-axis inductances $(\Delta L \neq 0)$ leads to the amplitudes of d_e and q_e high-frequency currents being dependent on the rotor position error angle θ_s in the estimated synchronous reference frame. In the case of zero position estimation error, the q_e-axis high-frequency current vanishes. After corresponding signal conditioning, this q_e-axis high-frequency component serves as the input of the position tracking observer for estimating rotor position and speed.

3.2. Improved Sliding Mode Observer

3.2.1. Sliding Mode Observer Design

Figure 1 illustrates the flow of the improved SMO designed in this paper, where Figure 1a presents the design flow of the conventional sliding mode observer:

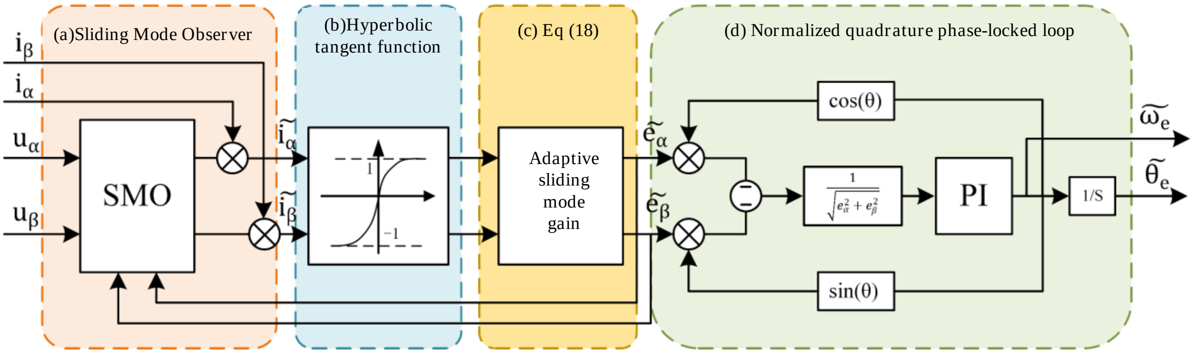

Figure 1. Improved SMO.

Rewriting the voltage equation of Equation (1) into the form of a current differential state equation:

$$\frac{d}{dt}\begin{bmatrix} i_\alpha \\ i_\beta \end{bmatrix} = \begin{bmatrix} -\frac{R_s}{L_d} & -\frac{(L_d - L_q)\omega_e}{L_d} \\ \frac{(L_d - L_q)\omega_e}{L_d} & -\frac{R_s}{L_d} \end{bmatrix}\begin{bmatrix} i_\alpha \\ i_\beta \end{bmatrix} + \frac{1}{L_d}\begin{bmatrix} u_\alpha \\ u_\beta \end{bmatrix} - \frac{1}{L_d}\begin{bmatrix} e_\alpha \\ e_\beta \end{bmatrix} \tag{12}$$

The estimated current mathematical model of the conventional SMO for IPMSM is:

$$\frac{d}{dt}\begin{bmatrix} \hat{i}_\alpha \\ \hat{i}_\beta \end{bmatrix} = \begin{bmatrix} -\frac{R_s}{L_d} & -\frac{(L_d - L_q)\omega_e}{L_d} \\ \frac{(L_d - L_q)\omega_e}{L_d} & -\frac{R_s}{L_d} \end{bmatrix}\begin{bmatrix} \hat{i}_\alpha \\ \hat{i}_\beta \end{bmatrix} + \frac{1}{L_d}\begin{bmatrix} u_\alpha \\ u_\beta \end{bmatrix} - \frac{1}{L_d}\begin{bmatrix} ksig(\hat{i}_\alpha - i_\alpha) \\ ksig(\hat{i}_\beta - i_\beta) \end{bmatrix} \tag{13}$$

where: $\hat{i}_\alpha$, $\hat{i}_\beta$ is the observed value of the stator current in the coordinate system; k is the SMO switching gain ($k > 0$); sig() switching function.

The sliding mode surface is defined as follows:

$$s = \begin{bmatrix} s_\alpha \\ s_\beta \end{bmatrix} = \begin{bmatrix} \tilde{i}_\alpha \\ \tilde{i}_\beta \end{bmatrix} = \begin{bmatrix} \hat{i}_\alpha - i_\alpha \\ \hat{i}_\beta - i_\beta \end{bmatrix} \tag{14}$$

The estimation error equation is given by:

$$\frac{d}{dt}\begin{bmatrix} s_\alpha \\ s_\beta \end{bmatrix} = \begin{bmatrix} -\frac{R_s}{L_d} & -\frac{(L_d - L_q)\omega_e}{L_d} \\ \frac{(L_d - L_q)\omega_e}{L_d} & -\frac{R_s}{L_d} \end{bmatrix}\begin{bmatrix} s_\alpha \\ s_\beta \end{bmatrix} + \frac{1}{L_d}\begin{bmatrix} e_\alpha - ksig(s_\alpha) \\ e_\beta - ksig(s_\beta) \end{bmatrix} \tag{15}$$

When the system reaches a steady state:

$$\begin{bmatrix} ksig(s_\alpha) \\ ksig(s_\beta) \end{bmatrix} = \begin{bmatrix} e_\alpha \\ e_\beta \end{bmatrix} = \psi_f \omega_e \begin{bmatrix} -\sin\theta_e \\ \cos\theta_e \end{bmatrix} \tag{16}$$

3.2.2. Switching Function Optimization

The switching control function adopted in the conventional SMO is discontinuous at the zero crossing, which gives rise to time and spatial lags in the control system. Furthermore, system inertia and measurement errors make the motion trajectory repeatedly cross the sliding mode switching surface, producing a sawtooth wave that leads to chattering during system operation [12]. As illustrated in Figure 1b, to tackle the chattering problem of the conventional switching function, this paper employs the hyperbolic tangent function tanh() depicted in Figure 2 to substitute for the conventional switching function sig().

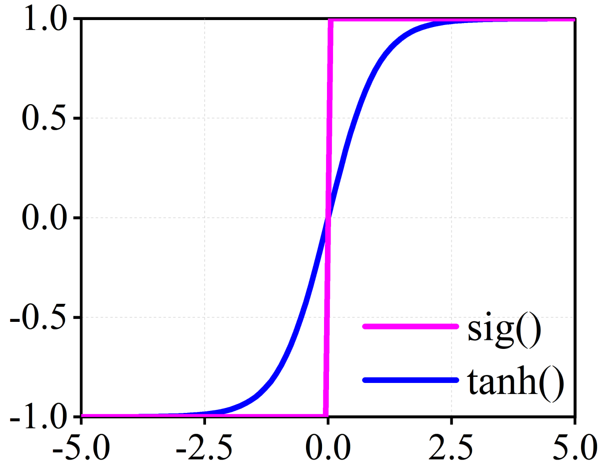

Figure 2. Optimized switching function.

3.2.3. Sliding Mode Gain Optimization

The sliding mode gain k dominates how rapidly the system responds dynamically, which can be clearly concluded from Equation (16). A larger gain yields a faster response speed, yet may also induce larger control input and chattering [13]. Therefore, this paper develops a new adaptive sliding mode gain optimization strategy that introduces the integral of the current error over the sampling period into the sliding mode surface, yielding:

$$S_n = \begin{bmatrix} S_\alpha \\ S_\beta \end{bmatrix} = \begin{bmatrix} \widetilde{i}_\alpha + G\int_0^t \widetilde{i}_\alpha d\tau \\ \widetilde{i}_\beta + G\int_0^t \widetilde{i}_\beta d\tau \end{bmatrix} \tag{17}$$

where G is a positive number, $0 < G <$ (Rs/Ld), to guarantee the stability of the sliding motion.

The adaptive sliding mode gain optimization algorithm depicted in Figure 1c is defined as follows:

$$k_n(t) = h\int_{t_0}^t \left(\left|S_n\right| - \eta k_n(t)\right) d\tau \tag{18}$$

$h > 0$ controls the adaptive gain's response: bigger h speeds up response but increases position error and noise. For $0 < \eta < 1$, small η amplifies gain and chattering; large η reduces gain and breaks the reaching condition, destabilizing the observer. Equation (18) yields a self-regulating, bounded adaptive gain $k_n(t)$ that maintains SMO stability across different operating points.

3.2.4. Position Tracking Observer Design

For sliding-mode observer sensorless control, arctangent and differential formulas directly solve rotor position and angular velocity.

$$\hat{\theta}_e = -\tan^{-1}\left(\frac{\hat{e}_\alpha}{\hat{e}_\beta}\right) \tag{19}$$

$$\widetilde{\omega}_e = \frac{d\theta_e}{dt} \tag{20}$$

However, positions calculated by Equations (19) and (20) are vulnerable to noise and harmonics. We employ the normalized quadrature PLL in Figure 1d for position/speed extraction. It removes the $\psi_f\omega_e$ component via normalization to mitigate speed transient disturbances, and delivers zero steady-state phase tracking to enhance estimation accuracy.

4. Switching Strategy

Since both HFI and SMO can only be applied within specific speed domains, a switching strategy is needed to accomplish full-speed domain motor operation. The simplest approach is the single-point switching method, setting a fixed switching point and altering the sensorless control algorithm when the speed reaches the switching point.

4.1. Weighted Switching Strategy

Several scholars proposed the weighted switching strategy [14], whose principle is depicted in Figure 3. A transition speed band is predefined. Within this range, the weight coefficient K regulates the HF injection voltage amplitude of pulsating HFI. As the estimated rotor speed grows, K decreases and the injection voltage amplitude declines accordingly. This variable-amplitude HF injection weakens interference to the SMO algorithm, improves full-speed sensorless control precision for PMSMs, and suppresses motor acoustic noise.

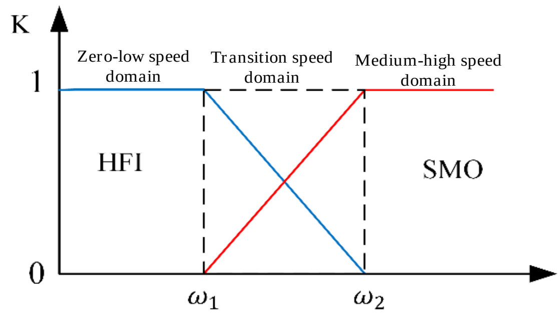

Figure 3. Weighted switching method.

4.2. Fuzzy Logic-Based Switching Strategy

Figure 4 illustrates the flowchart of the full-speed domain sensorless control strategy proposed in this paper. Building upon the conventional FOC control model, the sensorless algorithm and switching strategy are refined as follows: first, the speed domain is judged according to the current motor speed. HFI is applied in the zero-low speed region, and the improved SMO is applied in the medium-high speed region; in the transition-speed region, the weighted switching method is adopted. Since the weight coefficient K in the weighted switching strategy is linear, load disturbances on the motor during the switching interval may trigger speed oscillations. To alleviate the chattering caused by the linear weight coefficient, this paper incorporates a fuzzy logic controller (FLC) into the switching strategy, enabling adaptive adjustment of the weight coefficient throughout the weighted switching process.

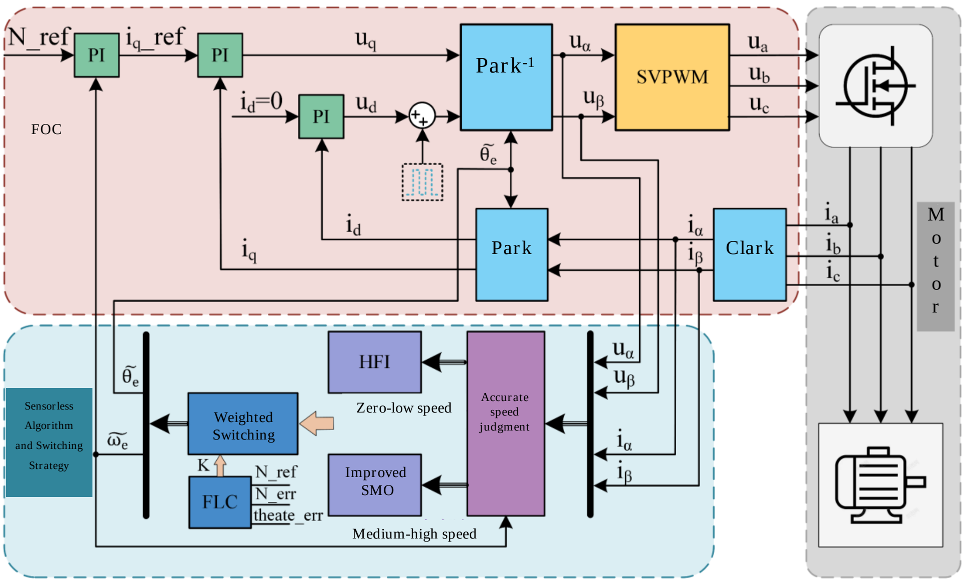

Figure 4. Block diagram of the full-speed domain sensorless control strategy based on fuzzy logic.

In the FLC, the reference speed N_ref, the absolute value of the speed difference between the two algorithm outputs (N_err), and the absolute value of the angle difference (theta_err) serve as inputs to the fuzzy controller, while the weight coefficient K is the output of the fuzzy controller.

The fuzzy sets of the input and output are defined as follows:

$$\text{N\_ref} = \{S, L\} \tag{21}$$

$$\text{N\_err} = \{NL, NS, ZO, PS, PL\} \tag{22}$$

$$\text{theate\_err} = \{NL, NS, ZO, PS, PL\} \tag{23}$$

$$\text{K} = \{S, L\} \tag{24}$$

where *S* stands for Small; *L* stands for Large; *NL* stands for Negative Large; *NS* stands for Negative Small; *ZO* stands for Zero; *PS* stands for Positive Small; *PL* stands for Positive Large.

Based on the switching interval speed and experience, the input universe N_ref of the fuzzy controller is determined as [300, 400]; the input universes N_err and theta_err are determined as [−10, 10]; and the output universe K [0, 1] of the input and output is determined as [0, 1]. The membership functions are shown in Figures 5 and 6.

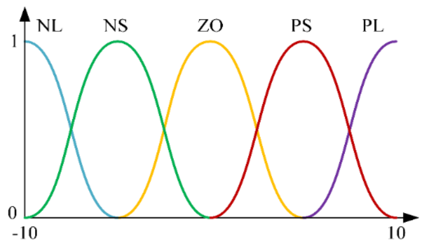

Figure 5. Membership function diagram of N_err and theate_err.

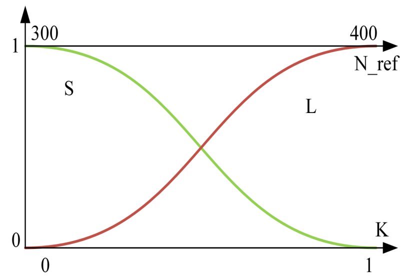

Figure 6. Membership function diagram of N_ref N_ref and K.

When the motor speed falls within the switching interval and N_ref and theate_err are small, the switching condition is met; when N_ref and theate_err are large, the switching is carried out after the observed angle converges. On the basis of this relationship, fuzzy rules are formulated, as listed in Table 1. The final output K is acquired through defuzzification using the centroid method.

Table 1. Fuzzy rule table.

	N_ref	N_err	theate_err	K
1	S	NL	NL	S
2	S	ZO	NL	S
3	S	ZO	ZO	L
4	L	NL	NL	S
5	L	ZO	ZO	L

5. Simulation and Experimental Results

A Matlab/Simulink simulation platform is constructed to verify the performance of the proposed improved strategy. This model adopts the FOC control framework shown in Figure 4, with detailed motor parameters tabulated in Table 2.

Table 2. Motor parameters.

Parameter	Definition	Value
R_s	Stator resistance (Ω)	0.958
L_d	d-axis inductance (mH)	5.25
L_q	q-axis inductance (mH)	12
ψ_f	Permanent magnet flux linkage (Wb)	0.1827
J	Moment of inertia (kg·m^2)	0.03
n_p	Number of pole pairs	4
n_N	Rated speed (rpm)	2000
T_N	Rated torque (N·m)	2
I_N	Rated current (A)	4

5.1. Simulation Verification of the Improved Sliding Mode Observer

First, simulation verification of the improved SMO is carried out. The system simulation time is 2 s, and the simulation step size is set to 2×10^{-7} s. The reference speed is configured as follows: the initial speed is 1000 rpm; at 1 s, the rotor speed abruptly shifts to 1500 rpm; at 1.5 s, the rotor speed abruptly changes to 1200 rpm. In the simulation experiment, the conventional SMO and the improved SMO are respectively applied to the PMSM closed-loop control. The speed response curves of the two methods are presented in Figure 7a. Compared with the conventional SMO, the improved SMO displays smaller speed fluctuations.

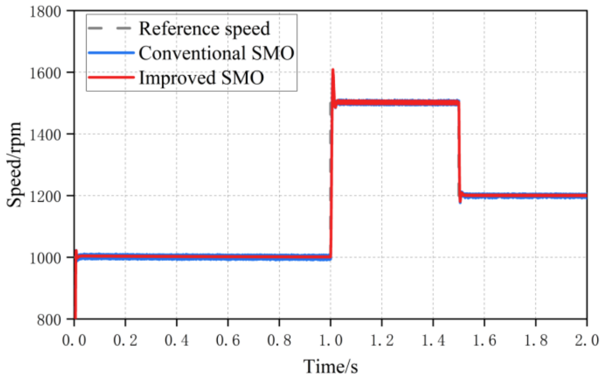

(a) SMO speed response

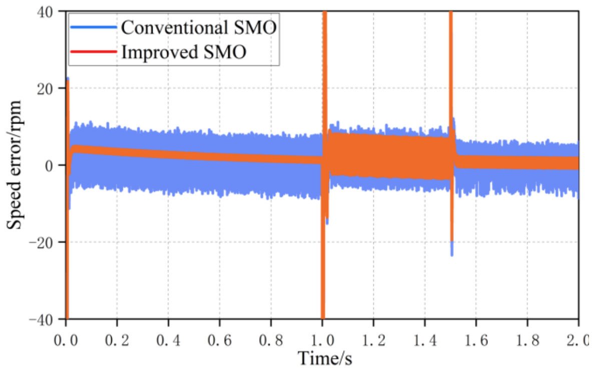

(b) SMO speed error

Figure 7. SMO simulation experiment results.

The reference speed and actual speed error curves of the two methods are presented in Figure 7b. The improved SMO displays chattering suppression effects at various speeds, cutting the error by up to approximately 75%.

5.2. No-Load Experiment of the Full-Speed Domain Sensorless Control Algorithm

The simulation time and step size stay unchanged, and the load is 0 N.m. The reference speed is configured as follows: at 1 s, the rotor speed accelerates to 1000 rpm and remains constant. In the simulation experiment, the single-point switching method, the weighted switching method, and the fuzzy logic switching method are respectively applied to the switching process. The speed response curves of the three methods are presented in Figure 8a. The single-point switching method selects a switching point of 400 rpm; when the speed reaches the switching point, a noticeable speed drop occurs, and the actual rotor speed converges to the reference speed after approximately 0.1 s. When the weighted switching method is adopted, the transition process does not display an obvious speed drop, yet large speed fluctuations still exist within the switching interval. When the fuzzy logic switching method is adopted, the transition process shows no speed drop, small fluctuations, and a smooth switching process.

The reference speed and actual speed error curves of the three methods are presented in Figure 8b. In both the zero-low speed region and the medium-high speed region, the actual speed can closely track the reference speed. In the transition speed region, the single-point switching method displays an obvious speed drop during switching; the weighted switching method can effectively suppress this speed drop; and the fuzzy switching method proposed in this paper can further cut the speed fluctuation by approximately 50%.

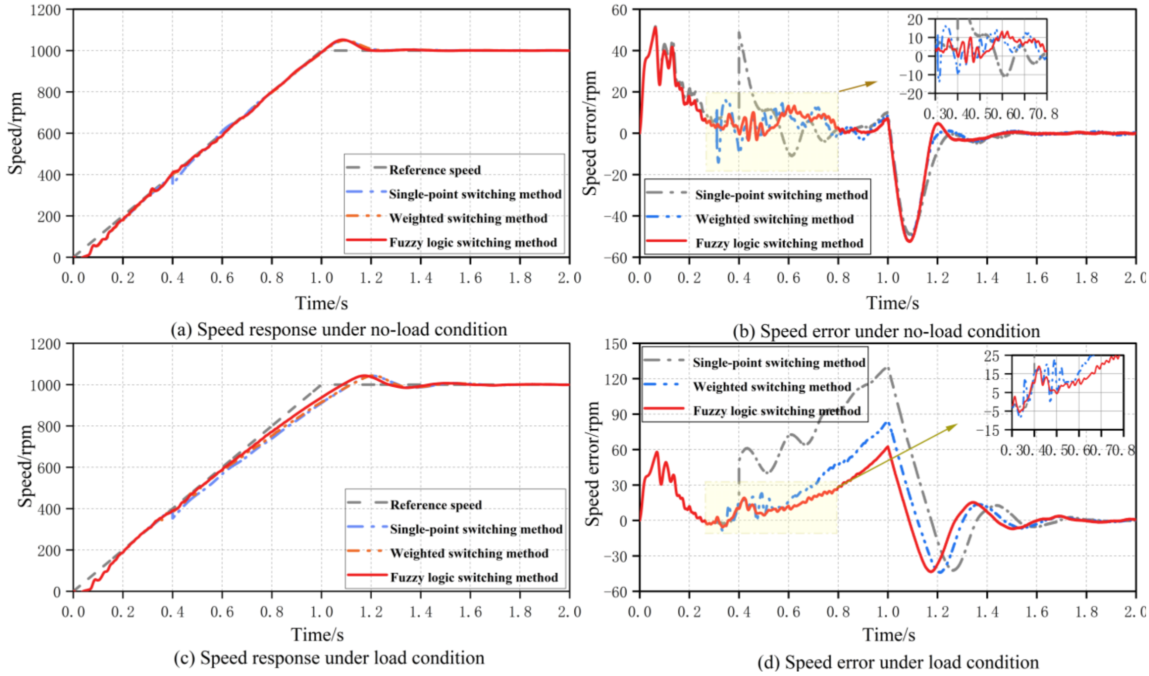

Figure 8. Full-speed-domain simulation experiment results.

5.3. Loaded Experiment of the Full-Speed-Domain Sensorless Control Algorithm

The speed simulation waveforms under constant speed and loaded operation are presented in Figure 8c. The load is set to 1 N.m, with all other settings unchanged. The single-point switching method displays an obvious speed drop during switching; due to the loaded operation, the actual speed converges to the reference speed approximately 0.6 s after the reference speed reaches 1000 rpm. The weighted switching method and the fuzzy switching method show no obvious speed drop, but display fluctuations within a certain range.

Based on the speed error curves in Figure 8d, it can be clearly observed that both the weighted switching method and the fuzzy switching method exhibit speed fluctuations in the transition speed domain. Compared with the weighted switching method, the fuzzy switching method reduces the speed fluctuation by approximately 30% and converges to the reference speed more quickly.

5.4. Experimental Verification

An experimental test bench (Figure 9) is built to verify the fuzzy logic switching-based sensorless PMSM control scheme proposed in this work.

In the full-speed domain experiment, the reference speed is configured as a ramp signal with a target speed of 1200 r/min. The lower limit of the switching interval is set to 300 r/min, and the upper limit is set to 400 r/min. The experimental results are presented in Figure 10. First, the single-point switching method is adopted with a switching threshold of 400 r/min; its speed response curve is presented in Figure 10a. After switching from HFI to SMO, the speed displays severe fluctuations, stabilizes after approximately 4 s, and the actual speed converges to the reference speed. The speed response curve of the weighted switching method is presented in Figure 10c; when entering the switching interval, the switching is accomplished in approximately 1.5 s, with speed fluctuations notably smaller than those of the single-point switching method, although some oscillation still remains. The speed response curve of the fuzzy-logic-based weighted switching method is presented in Figure 10e; when the speed reaches the switching interval, a smooth transition is achieved, and the switching is finished in approximately 1 s. Compared with the weighted switching method, it suppresses approximately 50% of the speed fluctuation.

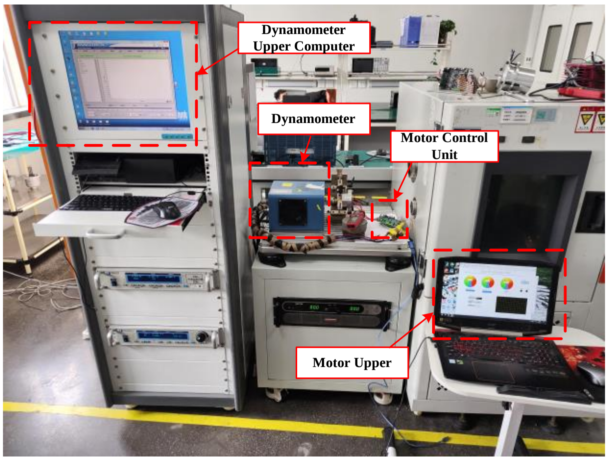

Figure 9. Experimental platform.

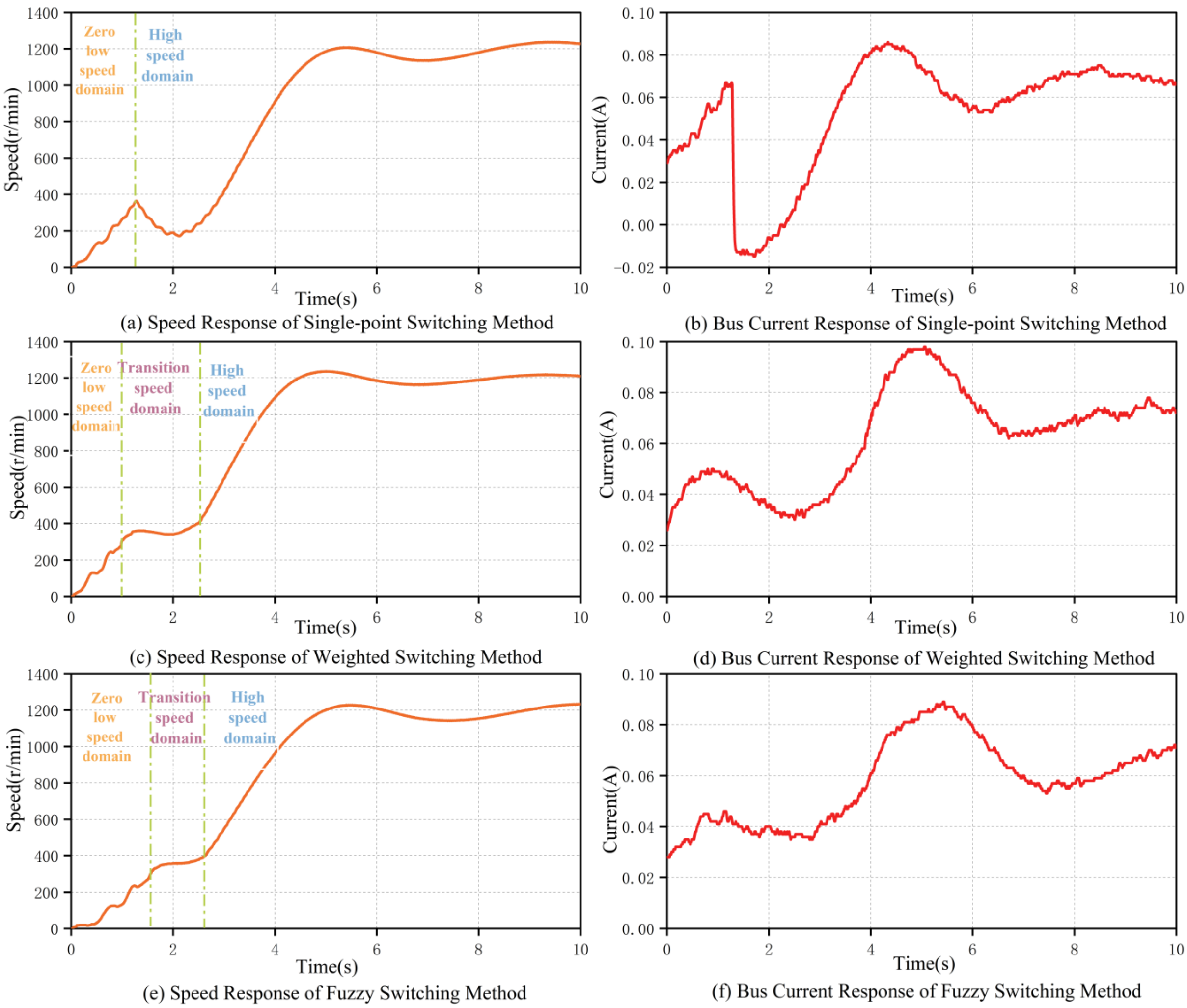

Figure 10. Full-speed-domain experimental results.

Figures 10b,d, f respectively present the DC bus current response curves of the single-point switching method, the weighted switching method, and the fuzzy-logic-based weighted switching method. It can be observed that since the single-point switching method employs forced switching, the bus current displays severe fluctuations when the observer changes. When the weighted switching method is adopted, the bus current fluctuation is partially suppressed, and the response becomes smoother, yet the fluctuation amplitude remains relatively large, with a fluctuation range of approximately ±0.01 A. When the fuzzy-logic-based weighted switching method is adopted, the bus current fluctuation is minimized, essentially stabilizing at approximately 0.04 A.

Table 3 lists the evaluation indicators of the three switching methods during the switching process. It can be seen that the fuzzy switching method displays the best performance. Compared with the ordinary weighted switching method, it cuts the switching time by 33.33%, the mean absolute speed deviation by 34.65%, the speed standard deviation by 36.20%, and the current range by 45%, which indicates that the system adopting the fuzzy-logic-optimized switching method is more stable. The experimental results confirm that employing the fuzzy-logic-optimized switching method to estimate the PMSM rotor speed attains higher estimation accuracy and enables smooth switching between different estimation methods within the switching speed domain.

Table 3. Switching process evaluation indicators.

Method	Time (s)	Mean Absolute Speed Deviation	Speed Standard Deviation	Current Range (A)
Single-point switching	-	-	-	0.080
Weighted switching	1.5	20.380	22.871	0.020
Fuzzy switching	1.0	13.318	14.591	0.011
Improvement ratio (%)	33.33	34.65	36.20	45.00

6. Conclusions

To tackle the problem that a single algorithm is unable to accomplish full-speed-domain motor operation, this paper puts forward a composite sensorless control algorithm strategy. Specifically, the pulsating high-frequency voltage signal injection method is adopted in the zero-low speed region, the improved sliding mode observer method is applied in the medium-high speed regions, and in the transition-speed region, the weighted switching method is employed, combined with a fuzzy logic controller to dynamically tune the output weights of the two control algorithms, thereby guaranteeing a smooth transition of the control strategy. Simulation results demonstrate the superiority of the improved sliding mode observer method proposed in this paper, which can cut the error by up to approximately 75%. The fuzzy-logic-based weighted switching method lowers speed fluctuations by approximately 50% under no-load conditions and approximately 30% under loaded conditions compared with the conventional weighted switching method. The final experimental results indicate that, compared with the weighted switching method, the switching time is reduced by 33.33%, the bus current range is reduced by 45%, and the speed fluctuation during switching is minimized.

Funding

Special Fund for Central Government Guidance to Local Authorities—Research and Application of High Power Density Axial Flux Integrated Electric Joints for Humanoid Robots, Grant No. 2025ZYDF094.

Author Contributions

Writing—original draft, J.D., H.L. and L.F.; writing—review and editing, J.D., H.L. and L.F. All authors have read and agreed to the published version of the manuscript.

Institutional Review Board Statement

Not applicable.

Informed Consent Statement

Not applicable.

Data Availability Statement

The datasets used and/or analysed during the current study available from the corresponding author on reasonable request.

Conflicts of Interest

The authors declare no conflict of interest.

References

1 Zhang L, Wang S, Bai J. Fast-Super-Twisting Sliding Mode Speed Loop Control of Permanent Magnet Synchronous Motor Based on SVM-DTC. *IEICE Electronics Express* 2021; **18**(**1**): 20200375.

2 Bianco E, Rubino S, Carello M, *et al.* Advanced Torque Control of Interior Permanent Magnet Motors for Electrical Hypercars. *World Electric Vehicle Journal* 2024; **15**(**2**): 46.

3 Li Y, Hu H, Shi P. A Review of Position Sensorless Compound Control for PMSM Drives. *World Electric Vehicle Journal* 2023; **14**(**2**): 34.

4 Zhang P, Shi Z, Yu B, *et al.* Research on a Sensorless ADRC Vector Control Method for a Permanent Magnet Synchronous Motor Based on the Luenberger Observer. *Processes* 2024; **12**(**5**): 906.

5 Zhang L, Dong Z, Zhao L, *et al.* Sliding Mode Observer for Speed Sensorless Linear Induction Motor Drives. *IEEE Access* 2021; **9**: 51202–51213.

6 Jinwu T, Lifan Z, Xinyun L, *et al.* Research on the Control Algorithm for a Brushless DC Motor Based on an Adaptive Extended Kalman Filter. *Sensors* 2026; **26**(**3**): 1050.

7 Zhang P, Ionel DM, Demerdash NAO. Saliency Ratio and Power Factor of IPM Motors With Distributed Windings Optimally Designed for High Efficiency and Low-Cost Applications. *IEEE Transactions on Industry Applications* 2016; **52**(**6**): 4730–4739.

8 Nair SV, Hatua K, Durga Prasad NVPR, *et al.* Quick and Seamless Transition Method for I-f to Sensorless Vector Control Changeover and On-the-Fly Start of PMSM Drives. *IET Electric Power Applications* 2020; **14**(**11**): 2231–2242.

9 Kumar P, Bottesi O, Calligaro S, *et al.* Self-Adaptive High-Frequency Injection Based Sensorless Control for Interior Permanent Magnet Synchronous Motor Drives. *Energies* 2019; **12**(**19**): 3645.

10 Yu Z, Zhang Y, Feng Y, *et al.* IPMSM Sensorless Control Technology Based on High Frequency Square Wave Injection Method. *Proceedings of SPIE* 2023; **12965**: 25–31.

11 Ning B, Zhao Y, Cheng S. An Improved Sensorless Hybrid Control Method of Permanent Magnet Synchronous Motor Based on I/F Startup. *Sensors* 2023; **23**: 635.

12 Li C. Rotor Position Estimation Algorithm for Surface-Mounted Permanent Magnet Synchronous Motor Based on Improved Super-Twisting Sliding Mode Observer. *Electronics* 2025; **14**: 436.

13 Xu W, Qu S, Zhao L, *et al.* An Improved Adaptive Sliding Mode Observer for Middle- and High-Speed Rotor Tracking. *IEEE Transactions on Power Electronics* 2021; **36**(**1**): 1043–1053.

14 Chen Z, Dawara AA, Zhang X, *et al.* Adaptive Sliding Mode Observer-Based Sensorless Control for SPMSM Employing a Dual-PLL. *IEEE Transactions on Transportation Electrification* 2022; **8**(**1**): 1267–1277.